CALCULATION OF HIGH-LIFT AERODYNAMICS ON ADAPTIVE UNSTRUCTURED GRIDS

A.R. JAHANGIRIAN and L.J. JOHNSTON

Department of Mechanical Engineering
UMIST, PO Box 88
Manchester, M60 1QD
United Kingdom

SUMMARY

A computational method is described which is generally-applicable to complex, two-dimensional, compressible aerodynamic flowfields at high Reynolds numbers. The method involves the use of unstructured grids to discretise the flow domain, which are generated in an essentially automatic manner. Techniques have been developed to produce grids which possess the required geometrical properties to enable accurate resolution of both inviscid flow and turbulent shear-flow regions. These grids are then further refined by adaptation to flow solutions of the Reynolds-averaged Navier-Stokes equations, using the two-equation k-ε turbulence model with wall-function type near-wall boundary conditions. Grid-generation procedures are described in some detail. Results are presented for the viscous transonic flow development around the SKF 1.1 aerofoil/manoeuvre flap configuration, for high-lift flow conditions involving severe shock-induced separation. Low-speed, high-lift computations for the NLR 7301 aerofoil/flap configuration are also presented. Generally good agreement with experiment is achieved for both cases, in terms of surface pressures and integrated loads, demonstrating the efficiency and accuracy of the present numerical method. It is noted, however, that the drag is somewhat over-predicted, which is partially attributed to the use of wall-function type boundary conditions.

1. INTRODUCTION

Mechanical high-lift devices, such as trailing-edge flaps and leading-edge slats, are used on civil transport aircraft to provide the additional lift necessary to fulfill the low-speed performance requirements associated with take off and landing. Similarly, in order to manoeuvre effectively at transonic speeds, the wing of a combat aircraft must be able to generate high lift without incurring an excessive drag penalty or the onset of buffet. Therefore, an accurate assessment of the aerodynamic performance of the high-lift system is an important part of the overall configuration optimisation process. The 1992 AGARD Conference on High-Lift System Aerodynamics[1] provides a useful survey of the various approaches being taken to the computation of high-lift system flowfields.

Considering for simplicity the two-dimensional flow case, deployment of high-lift devices results in a multi-element aerofoil configuration, whose flowfield is much more complex than that of a single aerofoil. In particular, the wakes from upstream elements can interact with the boundary layers on the upper surfaces of downstream elements. Such wake/boundary layer mixing promotes the development of thick viscous layers which may be highly-curved around maximum lift conditions, due to the large effective camber of the configuration. The wakes sitting above downstream aerofoil elements develop in streamwise pressure gradients which may be sufficiently strong to reverse the flow. These off-the-surface reverse-flow regions in wakes can grow in size to such an extent that they trigger large-scale flow separation on the upstream elements. This type of stall mechanism can result in a very sudden large loss of lift and increase in drag. A very perceptive discussion of the flow physics of multi-element, high-lift aerofoils is given by Smith[2].

Multi-element aerofoil, high-lift flows are complex from both a geometrical and flow physics point of view. For this reason, it appears likely that only numerical methods based on solution of the Reynolds-averaged Navier-Stokes equations will be able to deal with them in an adequate manner. It is also unlikely that simple algebraic turbulence models, needed to close the set of governing mean-flow equations, will prove to be adequate for the accurate prediction of the flow development through the stall. A more profitable approach will be to use turbulence models based on modelled transport equations, such as the well-known k-ε model of Launder and Spalding[3].

Additional complications are associated with the generation of a suitable computational grid for such a complex flow domain, which must also contain sufficient, well-placed grid-points so as to resolve all relevant flow features. Ideally, an essentially-automatic grid generation procedure is desirable, but the development of such methods into routine engineering tools remains as elusive as ever. The block-structured grid approach has proved to be highly-

successful, at least for the generation of grids applicable to inviscid flow computations. However, this approach does generally require extensive user intervention and expertise. Alternatively, unstructured grids can be generated around complex configurations in a relatively-straightforward manner. This approach also provides a natural environment for flow adaptation, whereby grid-points are placed in regions with high flow gradients to enhance the resolution and accuracy of the flow solution.

Rapid progress is being made in the development of fast and robust unstructured grid generators, but this work has focused mainly on inviscid-flow applications[4]. It is only recently that the problem of generating efficient unstructured grids for viscous flow applications has been addressed[5]-[8]. Such flowfields generally involve the presence of thin-shear layer regions adjacent to solid surfaces and in downstream wakes, both of which may have strong flow gradients in a direction normal to the main flow direction. The use of isotropic computational cells (which are optimal for the resolution of inviscid-flow regions) will lead to an unacceptable density of cells in the shear-layer regions. In fact, the resolution of high-Reynolds number turbulent flows requires the use of *highly-stretched* computational cells in boundary-layer and wake regions. Similarly, the highly-complex nature of turbulent aerodynamic flows at high Reynolds numbers points to a requirement to adapt the computational grid to the flow solution, so as to ensure the most efficient distribution of the grid-points.

The objective of the present work is the development of an essentially-automatic grid-generation procedure, aimed at high-Reynolds number turbulent flow applications for external aerodynamic configurations. Also, the incorporation of flow-adaptation techniques as an integral part of the grid-generation process has been planned from the outset, since this is considered to be the only viable technique to ensure adequate resolution of all relevant flow features. The grid-generation procedures are coupled to a flow solver based on the Reynolds-averaged Navier-Stokes equations and employing the k-ε transport-equation turbulence model. A detailed description of the grid-generation and flow-adaptation procedures is given in this paper. Results are presented for two aerofoil/flap configurations, indicating the performance of the method at transonic and low-speed flow conditions.

2. GRID GENERATION PROCEDURES

The present grid-generation method is based on a combination of grid-enrichment procedures, whereby new grid-points and point connectivities are created simultaneously[9]. A novel feature of the method is that it does not require an initial distribution of grid-points within the flow domain. Also, unlike the majority of existing methods, which start with a well-refined

discretisation of the geometry, the present approach adopts a very crude initial discretisation of the geometry and the outer boundary of the flow domain. Surface and field grids, of increasing resolution, are generated simultaneously as the cell sub-division process continues. The resulting unstructured grids are composed of triangular cells.

A cell-edge based data structure is produced by the grid-generation procedure, such a structure being compatible with existing flow solvers of the finite-volume type. However, an additional cell-based data structure is employed during the grid-generation process, so that searches through the list of cell-edges are not required. This results in a very efficient grid-generation procedure, which can produce satisfactory grids within a matter of seconds on a computer work-station.

2.1 Isotropic Grid Generation

Fig. 1(a) shows a typical starting grid for a computational domain which contains two circles. The grid contains only 4 points on each circle and 8 points on the outer boundary. These grid-points are connected together to produce an initial discretisation of the flow domain into triangular cells which, for this case, consists of only 18 cells, 35 cell-edges and 18 vertices. Once the starting grid is constructed, the computational cells are successively sub-divided using the method developed by Jahangirian and Johnston[9]. Effective generation of isotropic (equilateral) cells is achieved by using directional sub-division combined with grid-point movement. In particular, enrichment of the grid is based on the sub-division of the longest edge of a targeted cell, with checks to ensure that the aspect ratio of adjacent cells is not increased, Fig. 2(a).

Preliminary clustering of cells around the geometry is performed by introducing point and/or line sources within the flow domain, as appropriate. Subsequently, a desired distribution of the cell-edge length scale is defined which provides a constraint for the cell sub-division process whilst producing small cells in the vicinity of the geometry. Grid-point movement is also used in the early stages of the refinement process to effectively draw the grid-points towards to the sources. This is implemented through a Laplacian-type smoothing procedure, incorporating a weighting-function which is inversely-proportional to the desired length scale at each grid-point. To ensure the integrity of the geometry boundaries, parametric cubic splines are used when defining a new surface grid-point. Grid quality is further improved by using an edge-swapping routine, whereby the common edge to adjacent cells is swapped between vertices so as to decrease the aspect ratios of the cells. A computational grid of satisfactory quality and resolution is normally achieved after 20 cycles of the grid-refinement procedure. Fig. 1(b) shows the grid around the two circles after this second stage of the grid generation procedure. Cells have been clustered around the

geometry elements by using a point source at the centre of each circle.

Fig. 3 shows a typical grid resulting from the present inviscid grid-generation procedure, for a more representative four-element aerofoil system in a landing configuration. The grid contains 7565 cells, 11533 cell-edges (including 313 surface edges) and 3965 vertices.

2.2 Viscous Flow Regions

There are three main stages to the grid-generation procedure for viscous-flow applications:

1. Generation of a Starting Grid
2. Grid Generation for Inviscid Flow Regions
3. Grid Generation for Viscous Flow Regions

The initial starting grid is generated in a similar manner as for inviscid-flow applications, except that a layer of regularly-triangulated cells is wrapped around each geometry element and extended downstream. These regions encompass the expected boundary-layer and wake regions. The grid-points forming the outer edge to these regions are connected to points on the outer boundary. Fig. 4(a) shows the initial starting grid for the SKF 1.1 two-element aerofoil/manoeuvre flap configuration, to be considered in the results section below. Following the procedure outlined in the previous section, the computational cells *external* to the viscous grid regions are directionally sub-divided to produce isotropic cells, suitable for the resolution of inviscid-flow regions. Grid-points are further clustered around point/line sources using grid-point movement. The grid after this stage of the procedure is shown in Fig. 4(b). Note that the computational grid now provides an adequate resolution of the aerofoil geometries, without having had to explicitly discretise the surface geometry beforehand.

Having generated the grid outside the anticipated viscous shear-layer regions, the final step is to refine the inner regions so as to obtain an adequate resolution of the boundary layers and wakes. Within such regions, it is flow gradients *across* the viscous layers which dominate the flow development. Therefore, cell sub-division within the viscous layer regions proceeds in an anisotropic manner, so as to produce the required high-aspect ratio, regularly-triangulated cells. Grid refinement is carried out by introducing new grid-points on the cell-edges normal to the geometry and systematically connecting the points to keep the regularity of the grid in the viscous layer regions, Fig. 2(b). Increased near-surface resolution can be obtained by using a geometrical stretching function to cluster the grid-points close to the geometry.

Fig. 4(c) shows the computational grid resulting from this final stage of the grid-generation procedure, which is now ready for use by the flow solver. The grid contains 11660 cells, 17663 cell-edges (including 314 surface edges) and 6002 vertices. The grid-generation procedure was implemented on an HP-735 (125 MHz) computer workstation. The total required CPU time, including grid generation and input/output operations, was only 4.54 seconds which gives some indication of the efficiency of the present approach.

2.3 Flow Adaptation

The grid-generation procedure outlined above results in a computational grid that is adequate for an initial viscous flow solution since the boundary layer and wake regions are effectively resolved. However, the grid may not yet be sufficiently well-refined to give the required resolution of flow features such as shock waves and separated shear layers. Obviously, the positions of these physical flow features can move as a result of a change in flow conditions (e.g. Mach number, Reynolds number and incidence angle). Therefore, a new grid would need to be generated for each flow condition, to maintain a consistent level of flow resolution. This requirement can be fulfilled most efficiently by further refining the initial grid, by adapting it to an initial flow solution. In the present approach, the grid is adapted to the flow solution by refining it in high flow-activity regions using the cell sub-division techniques already presented. However, in this case, the cells are targeted for sub-division based on the magnitude of flowfield gradients obtained from the initial flow solution.

Static pressure gradients and total pressure-loss gradients are used to detect inviscid (shock waves and stagnation points) and viscous (boundary layers and wakes) flow features respectively. To accomplish this, a flow-gradient indicator is computed for each cell-edge, by taking the first difference of the relevant flow property along that edge, made non-dimensional by the cell-centre value. The cell is then targeted for refinement if the indicator exceeds a pre-set threshold value (typically in the range 0.02-0.05). Since adequate resolution of the boundary layer and wake regions is generally already provided through the initial grid-generation procedure, grid-adaptation to viscous flow features is restricted to separated shear layers. This is achieved by scaling the viscous flow-feature detector with the magnitude of the smallest edge-length of the cell. In this way, those cells in the fully-attached flow regions, with small edge-lengths normal to the geometry, will not be further refined. Fig. 4(d) shows a typical computational grid adapted to a viscous transonic flow solution for the SKF 1.1 aerofoil/flap configuration. The corresponding iso-Mach number contours before and after flow adaptation are shown in Figs. 5(a) and (b) respectively. Note that the strong upper surface shock wave present at this flow condition induces an extensive separation of the main aerofoil boundary layer. The solution obtained on the flow-

adapted grid, Fig. 5(b), indicates a much-improved resolution of both the shock wave and the separated boundary layer.

3. VISCOUS FLOW SOLVER

The governing mean-flow equations are the Reynolds-averaged Navier-Stokes equations applicable to compressible, turbulent flow at high Reynolds numbers. A turbulence model is required to close the set of mean-flow equations, modelling the additional Reynolds-stress terms that appear due to the time-averaging procedure applied to the governing equations. For the results presented below, the two-equation k-ϵ model of Launder and Spalding[3] is used. This model introduces a turbulent viscosity coefficient (in analogy to the molecular viscosity coefficient) to replace the Reynolds-stress terms. The local value of the turbulent viscosity coefficient is evaluated using the local values of the turbulent kinetic energy k and its rate of dissipation ϵ, obtained from the two modelled transport equations. The so-called wall-function approach is adopted to treat the near-wall region of the boundary layers. No attempt is made to model explicitly the molecular-viscosity dominated region immediately adjacent to the surface. Instead, the solution is 'patched' to the semi-logarithmic law-of-the-wall in the fully-turbulent region. This approach is computationally very efficient, since a highly-refined computational grid is not required in the near-wall region.

The mean-flow and turbulence-transport equations are solved in time-dependent integral form, marching the unsteady flow equations in time to a steady-state solution. For transonic flows, this enables the method to resolve both subsonic and supersonic flow regions without any changes to the numerical algorithm. The governing flow equations are first discretised in space using a cell-centred, finite-volume procedure. The resulting set of semi-discrete equations is then marched in time using an explicit, multi-stage scheme. Further details of the present numerical method can be found in Johnston and Stolcis[10].

The convective transport terms in the mean-flow equations are discretised using a second-order accurate, centred finite-volume scheme. Such an approach will not necessarily suppress oscillations that may develop in the flow solution during the transient phase before the steady-state is achieved. Therefore, additional numerical dissipation terms are explicitly-added to the mean-flow equations to damp any such oscillations. These terms are a blending of second- and fourth-differences of flow variables, the former to ensure clean capture of shock waves and the latter to provide a background level of smoothing. Since these numerical dissipation terms are diffusive in nature, they can significantly influence the development of the viscous layers. Scaling of these terms within viscous-layer regions is applied, to ensure that the physical diffusive processes are not corrupted by the numerical diffusion; see Cantariti[11] for a detailed description of our approach to the treatment of the numerical dissipation terms. The convective transport terms of the two turbulence-transport equations are discretised using a first-order, upwind finite-volume scheme and so require no additional numerical dissipation terms.

4. RESULTS

Two aerofoil/trailing-edge flap configurations are considered in this section, to demonstrate the predictive capability of the present method at both low-speed and transonic high-lift flow conditions.

SKF 1.1 Aerofoil/Manoeuvre Flap

Fig. 4(c) shows the SKF 1.1 transonic aerofoil/manoeuvre flap configuration of Stanewsky and Thibert[12]. The 25% chord flap is deflected 10°, this being referred to as configuration 5 in the AGARD data report[12]. The aerofoil/flap configuration was tested over a wide range of transonic flow conditions in the DFVLR 1 x 1 Meter Transonic Tunnel, at a freestream Reynolds number of about 2.2 x 10^6 with free transition on both aerofoil elements. Stolcis and Johnston[13] carried out a detailed set of computations for this experimental data-set, using an earlier version of the present computational method. It was concluded that there were some problems with the wind-tunnel wall corrections to be applied to the experimental data, as detailed in the data-report[12]. Subsequently, Haase[14] provided additional information on corrections to the freestream Mach number and incidence angle. He also made available additional experimental data at more extreme flow conditions.

Transition was fixed on both aerofoil elements for the present computations, at 3% and 25% chord respectively on the upper and lower surfaces of the main aerofoil, and at the leading edge of the flap. All computations began from an initial flow solution on the starting grid shown in Fig. 4(c). For each flow condition considered, the computational grid was adapted to both the inviscid and viscous flow features of this initial solution. A second flow solution was then obtained on the flow-adapted grid.

Fig. 8 shows the results obtained for three incidence angles at a nominal freestream Mach number of 0.76, all cases involving some degree of shock-induced flow separation. The flow-adapted grids also show clearly the improved resolution of both the shock waves and separated boundary layers. The predicted surface pressure distributions for all cases agree well with experiment, considering the severity of the flow conditions. Note that the upstream movement of the shock wave with

increasing incidence angle, as the separated-flow region develops in extent, is well-predicted.

The variation of integrated loads with incidence angle is shown in Fig. 9, indicating very good agreement between predictions and experiment for the lift coefficient and pitching-moment coefficient. The drag coefficient is substantially over-predicted by the present method, a result that is partially attributable to the use of wall-function near-wall boundary conditions. However, examination of the surface pressure distributions indicates that the predicted shock waves are always too strong, suggesting that the use of the k-ϵ, turbulent-viscosity based, turbulence model leads to an underprediction of the shock wave/boundary layer interaction.

NLR 7301 Aerofoil/Flap

The second configuration to be considered is the NLR 7301 low-speed, high-lift aerofoil/flap of van den Berg[15]. Fig. 10 shows the computational grid obtained by the present grid-generation procedures, containing 12502 cells, 18890 cell-edges and 6387 vertices. An initial flow solution was obtained on this grid at a freestream Mach number of 0.185, Reynolds number of 2.51 x 10^6 and an incidence angle of 13.1°. These conditions are just below the maximum lift point for this configuration. The computational grid was then adapted to the initial flow solution. Fig. 11, in particular, shows the influence of grid-adaptation in the large pressure-gradient region near the leading edge of the main aerofoil. The predicted surface pressure and skin friction distributions, Fig. 12, agree well with experiment for this case, even for the initial flow solution on the unadapted grid. However, flow adaptation does lead to some improvement in predicted skin friction levels over the first 50% of the main aerofoil upper surface. Finally, the Mach number and total-pressure loss contours shown in Fig. 13 indicate the smoothness of the predicted flowfield solution.

Current work is focused on a more extensive evaluation of the present method when applied to low-speed, high-lift, multi-element aerofoil configurations. Two areas in particular are being addressed. The performance of a differential Reynolds-stress model (DRSM), to replace the turbulent-viscosity based k-ϵ model, is under evaluation. Such a turbulence model solves modelled transport equations for the Reynolds stresses themselves, which are retained in exact form in the mean-flow equations. Preliminary results by Cantariti and Johnston[16], using unadapted computational grids, indicate a substantial improvement in the predicted stall development for low-speed, high-lift flows. The second area of current work is the replacement of the wall-function near-wall boundary conditions with a turbulence model that will enable flow computations right down to the surface of the aerofoil elements. An improvement in the predicted drag levels is

expected with these near-wall turbulence modelling modifications.

5. CONCLUSIONS

An essentially-automatic procedure for computational grid generation and flow solution for two-dimensional, high-lift aerofoil configurations has been described. The Reynolds-averaged Navier-Stokes equations are solved in conjunction with a two-equation turbulence model. Resolution of both viscous and inviscid flow features is enhanced by adapting the computational grid to an initial flow solution. Results presented for transonic and low-speed, high-lift aerofoil/flap configurations demonstrate the efficiency of the grid-generation procedures and indicate that predictions agree well with experiment. In particular, the predictions show the correct upstream movement of shock-wave position with increasing incidence angle as transonic shock-induced boundary layer separation develops on an aerofoil/manoeuvre flap configuration.

ACKNOWLEDGEMENTS

REFERENCES

[1] AGARD CP.515, 'High-Lift System Aerodynamics', September 1993

[2] Smith, A.M.O., 'High-Lift Aerodynamics', AIAA Paper 74-0939, 1974

[3] Launder, B.E. and Spalding, D.B., 'The Numerical Computation of Turbulent Flow', Computer Methods in Applied Mechanics and Engineering, Vol.3, March 1974, pp.269/289

[4] Jameson, A., Baker, T.J. and Weatherill, N.P., 'Calculation of Inviscid Transonic Flow Over a Complete Aircraft', AIAA Paper 86-0103, 1986

[5] Mavriplis, D.J., 'Euler and Navier-Stokes Computations for Two-Dimensional Geometries Using Unstructured Meshes', ICASE Report 90-3 (also NASA CR 181977), 1990

[6] Pirzadeh, S., 'Unstructured Viscous Grid Generation by Advancing Layers Method', AIAA Paper 93-3453, 1993

[7] Hassan, O., Probert, E.J., Morgan, K. and Peraire, J., 'Line Relaxation Methods for the Solution of 2D and 3D Compressible Flows', AIAA Paper 93-3366, 1993

[8] Marchant, M.J. and Weatherill, N.P., 'Unstructured Grid Generation for Viscous Flow Simulations', Proceedings of the 4th Conference on Numerical Grid Generation in CFD and Related Fields, pub. Pineridge Press, 1994, pp.151/162

[9] Jahangirian, A.R. and Johnston, L.J., 'Unstructured Grid Generation and Flow Adaptation for External Aerodynamic Flows', Numerical Methods for Fluid Dynamics V, Morton, K.W. and Baines, M.J. (Eds.), pub. Oxford University Press, 1995, pp.439/445

[10] Johnston, L.J. and Stolcis, L., 'Prediction of the High-Lift Performance of Multi-Element Aerofoils Using an Unstructured Navier-Stokes Solver', AGARD CP.515, 'High-Lift System Aerodynamics', September 1993, pp.13-1/13-18

[11] Cantariti, F.J.-J., 'Computation of External Aerodynamic Flows Using Differential Reynolds-Stress Modelling and Unstructured Grids', PhD thesis, Department of Mechanical Engineering, UMIST, 1995

[12] Stanewsky, E. and Thibert, J.J., 'Airfoil SKF 1.1 with Maneuver Flap', AGARD AR.138, May 1979, A5-1/A5-29

[13] Stolcis, L. and Johnston, L.J., 'Application of an Unstructured Navier-Stokes Solver to Multi-Element Airfoils Operating at Transonic Maneuver Conditions', AIAA Paper 92-2638-CP, June 1992

[14] Haase, W., Daimler-Benz Aerospace, private communication

[15] van den Berg. B., 'Boundary Layer Measurements on a Two-Dimensional Wing With Flap', NLR TR 79009 U, 1979

[16] Cantariti, F.J.-J. and Johnston, L.J., 'High-Lift Navier-Stokes Computations on Unstructured Grids Using a Differential Reynolds Stress Model', Numerical Methods for Fluid Dynamics V, Morton, K.W. and Baines, M.J. (Eds.), pub. Oxford University Press, 1995, pp.319/325
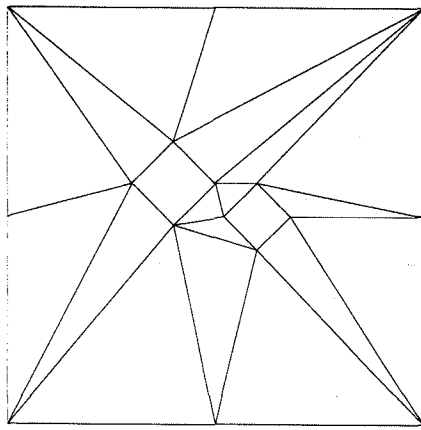
(a) Initial starting grid
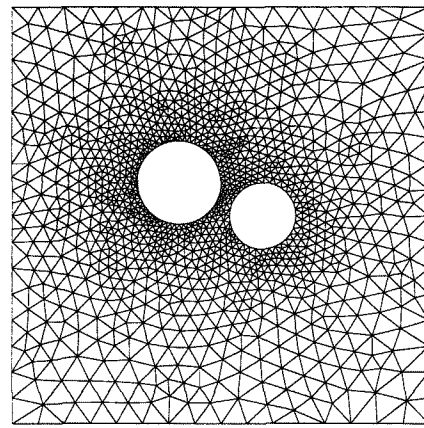
(b) Final grid

Figure 1   Isotropic grid generation procedure
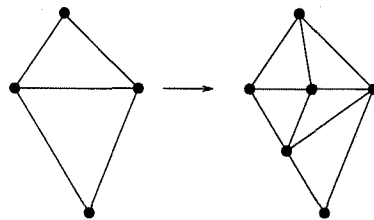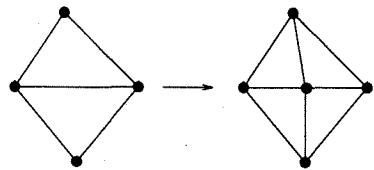
(a) Inviscid region
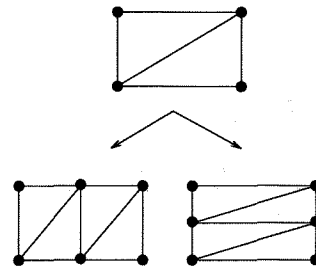
(b) Viscous region

Figure 2   Grid refinement strategies
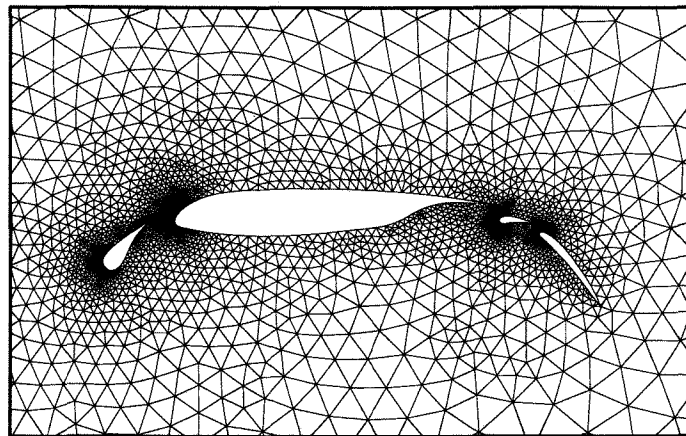
Figure 3   Inviscid Grid for 4-element landing configuration
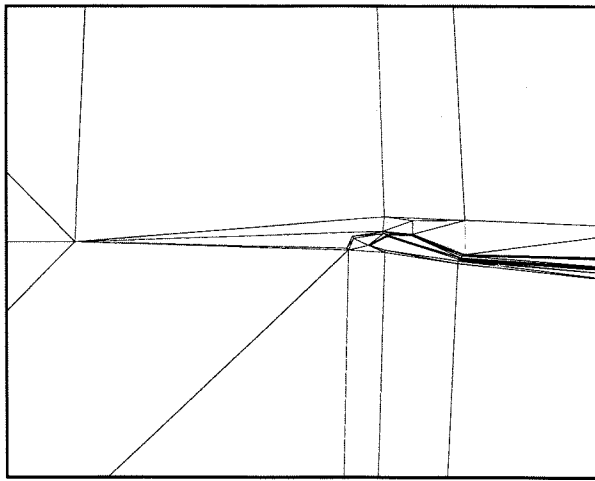
(a) Initial starting grid
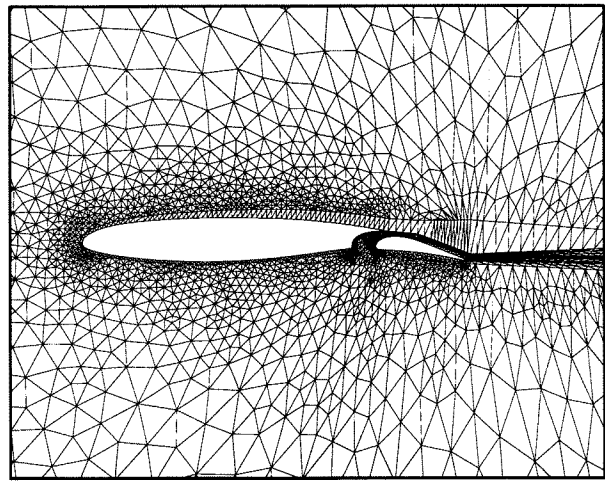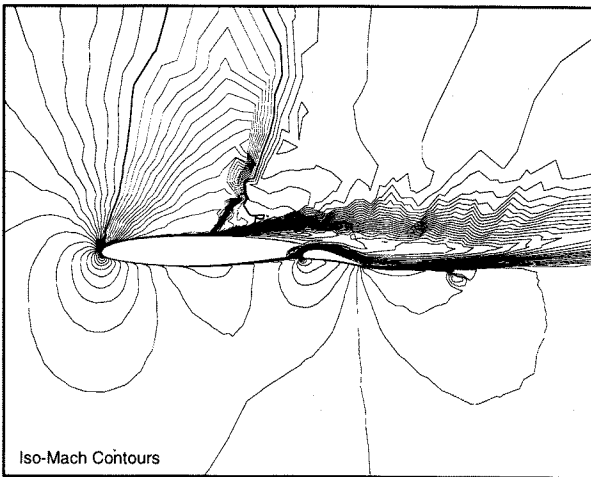

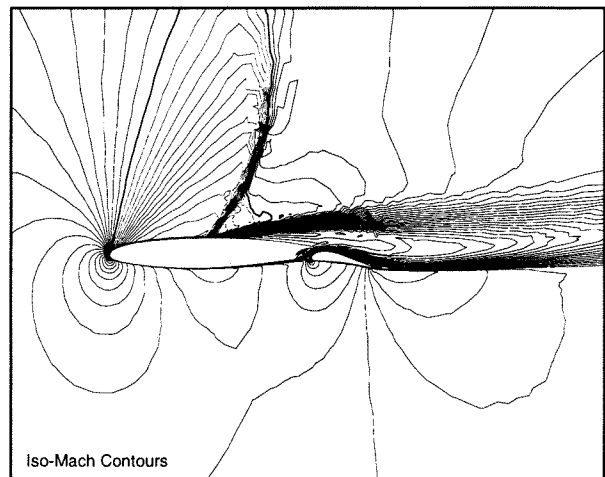(b) Grid after inviscid cell refinement
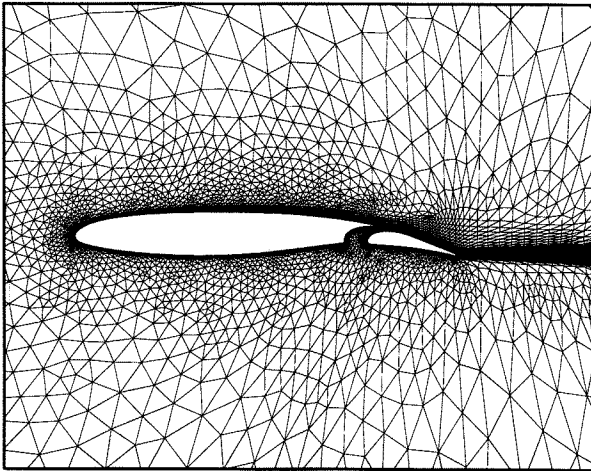
(c) Final viscous grid
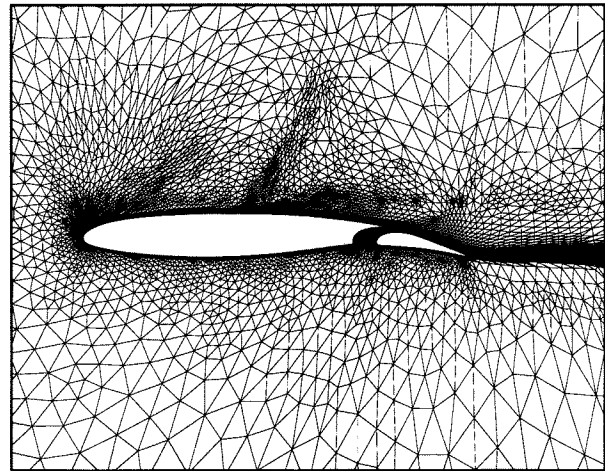
(d) Flow-adapted grid, Case 244

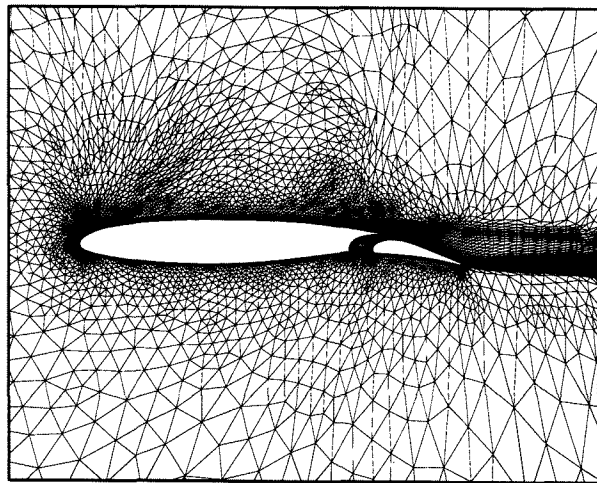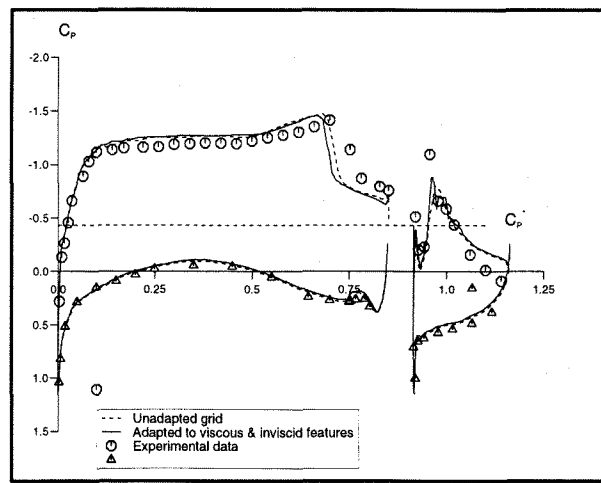Figure 4   Unstructured grid generation procedure for SKF 1.1

(a) Unadapted grid

(b) Adapted grid

Figure 5   Iso-Mach contours for SKF 1.1, case 244

2228

a) Flow-adapted grid

b) Surface pressures

Figure 6   SKF 1.1, Case 241 - $\alpha = 1.44^o$
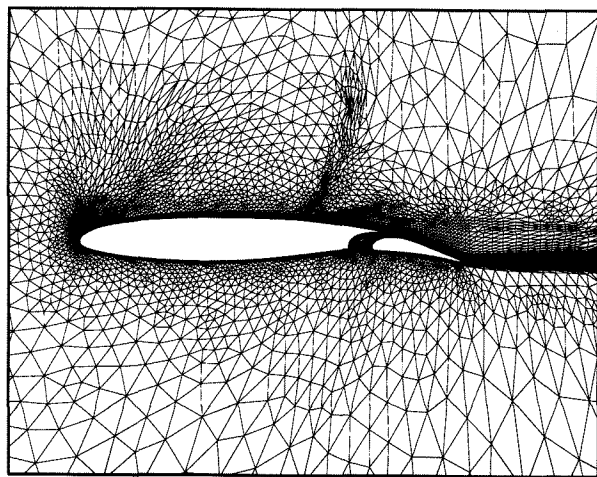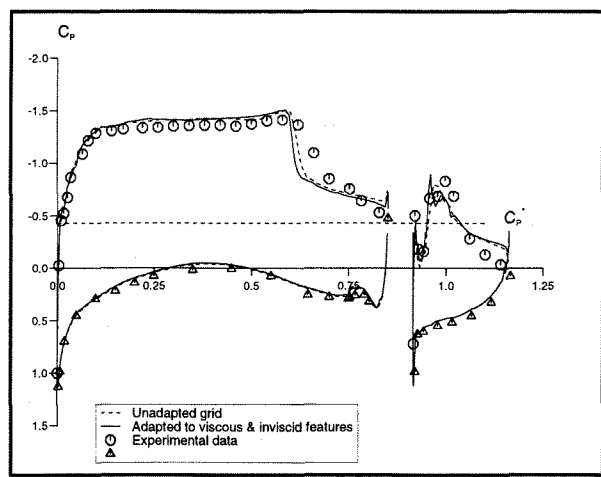
a) Flow-adapted grid

b) Surface pressures

Figure 7   SKF 1.1, Case 242 - $\alpha = 3.32^o$
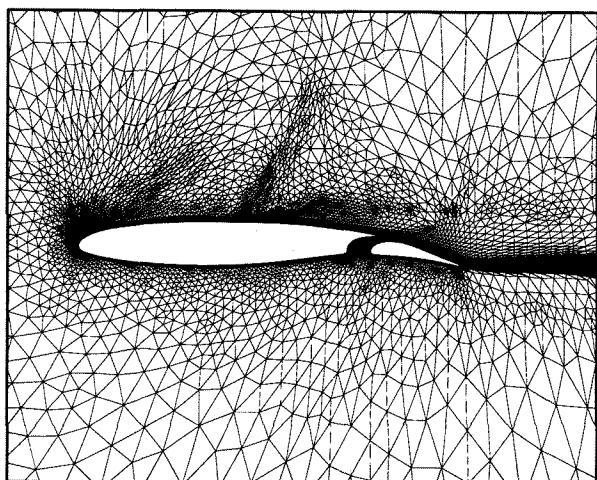
a) Flow-adapted grid
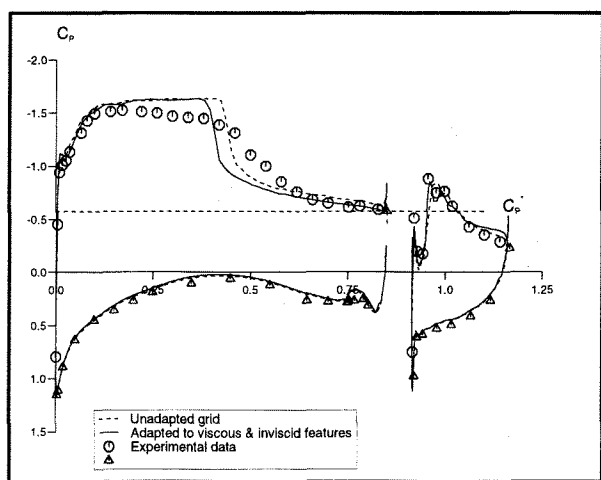
b) Surface pressures

Figure 8   SKF 1.1, Case 244 - $\alpha = 6.27^o$
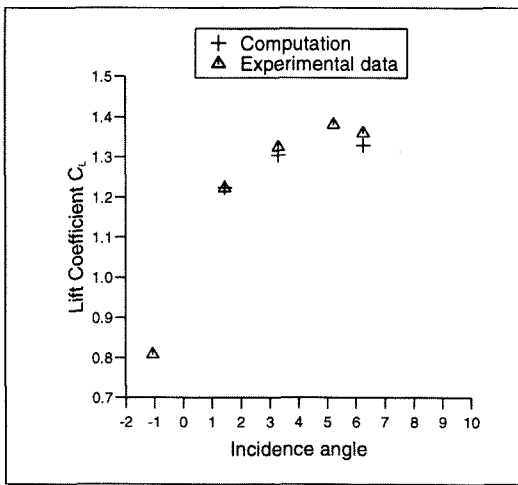
(a) Lift coefficient
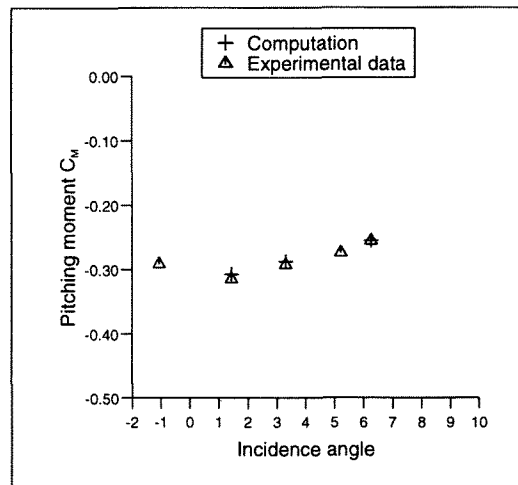
(b) Pitching moment coefficient
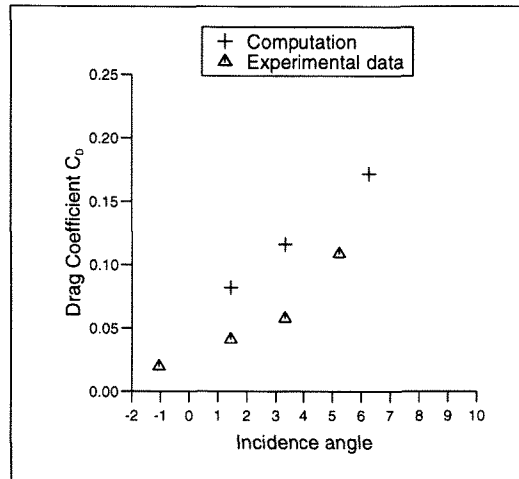
(c) Drag coefficient

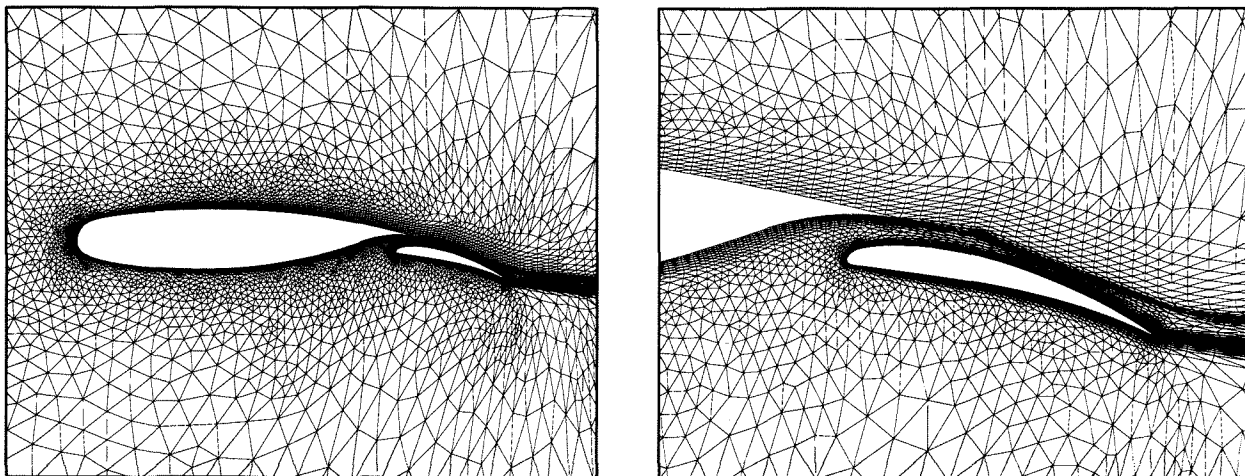Figure 9   Integrated loads versus incidence angle for SKF 1.1
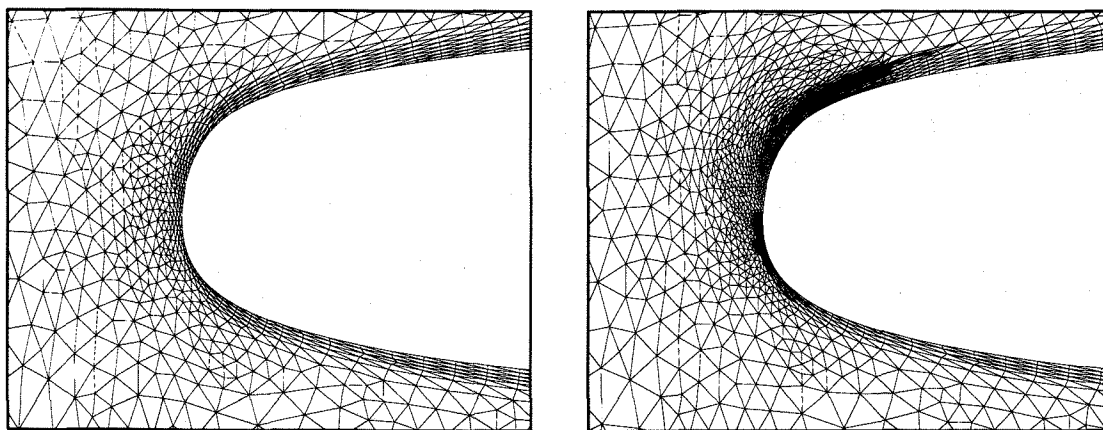

Figure 10   Final grid around NLR 7301 aerofoil/flap configuration

a) Unadapted grid   b) Adapted grid

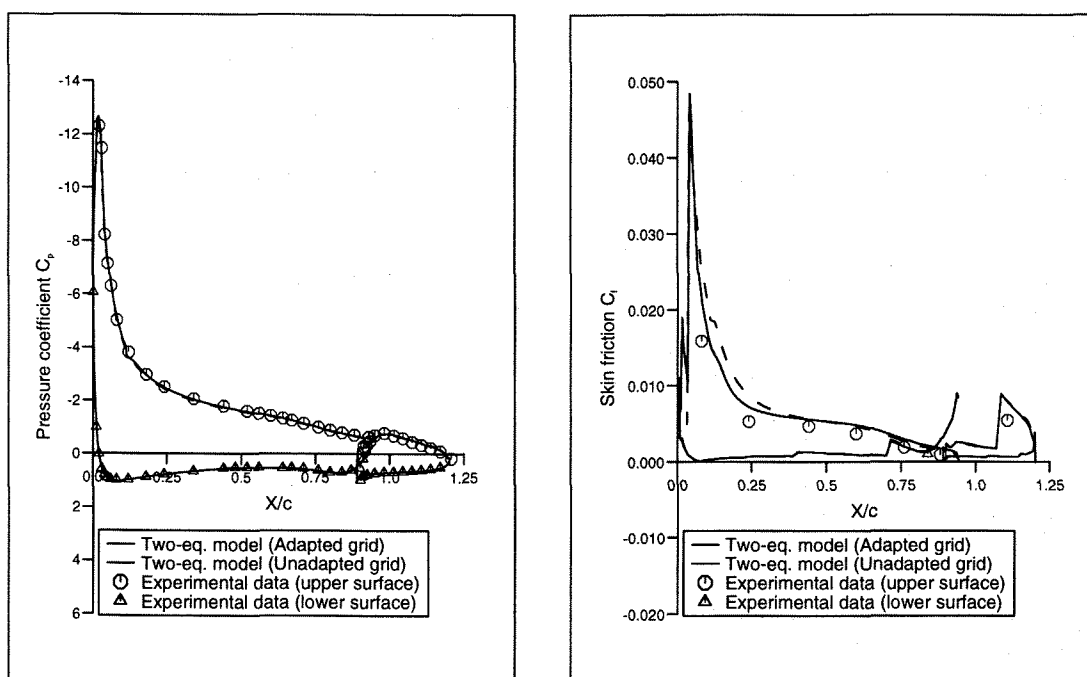Figure 11   Close-up of the leading edge

Figure 12   Surface pressure and skin friction distributions - NLR 7301, $\alpha = 13.1^o$
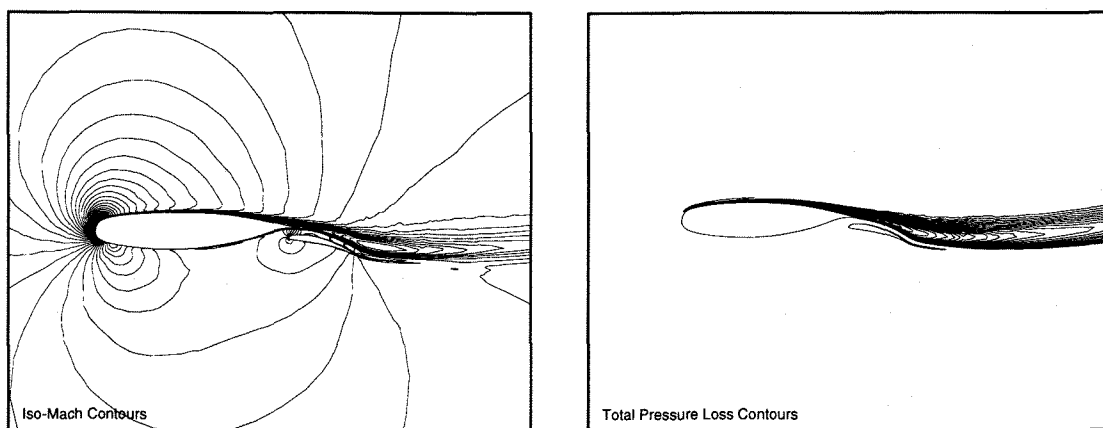

Figure 13   Iso-mach and total pressure loss contours, $\alpha = 13.1^o$